Hepatic Vessel Segmentation for 3D Planning of Liver Surgery:

Experimental Evaluation of a New Fully Automatic Algorithm

Francesco Conversano, PhD, Roberto Franchini, MSc,
Christian Demitri, PhD, Laurent Massoptier, MSc, Francesco Montagna,
Alfonso Maffezzoli, PhD, Antonio Malvasi, MD, Sergio Casciaro, PhD

Rationale and Objectives: The aim of this study was to identify the optimal parameter configuration of a new algorithm for fully automatic segmentation of hepatic vessels, evaluating its accuracy in view of its use in a computer system for three-dimensional (3D) planning of liver surgery.

Materials and Methods: A phantom reproduction of a human liver with vessels up to the fourth subsegment order, corresponding to a minimum diameter of 0.2 mm, was realized through stereolithography, exploiting a 3D model derived from a real human computed tomographic data set. Algorithm parameter configuration was experimentally optimized, and the maximum achievable segmentation accuracy was quantified for both single two-dimensional slices and 3D reconstruction of the vessel network, through an analytic comparison of the automatic segmentation performed on contrast-enhanced computed tomographic phantom images with actual model features.

Results: The optimal algorithm configuration resulted in a vessel detection sensitivity of 100% for vessels > 1 mm in diameter, 50% in the range 0.5 to 1 mm, and 14% in the range 0.2 to 0.5 mm. An average area overlap of 94.9% was obtained between automatically and manually segmented vessel sections, with an average difference of 0.06 mm^2. The average values of corresponding false-positive and false-negative ratios were 7.7% and 2.3%, respectively.

Conclusions: A robust and accurate algorithm for automatic extraction of the hepatic vessel tree from contrast-enhanced computed tomographic volume images was proposed and experimentally assessed on a liver model, showing unprecedented sensitivity in vessel delineation. This automatic segmentation algorithm is promising for supporting liver surgery planning and for guiding intraoperative resections.

Key Words: Liver; automatic vessel segmentation; liver surgery; computer-based surgery planning; rapid prototyping.

©AUR, 2011

R ecent literature has highlighted the need for methods that allow planning liver operations on the basis of individual patient data (1). The liver has a complex internal anatomy, which in some cases may differ notably from commonly adopted schematic classifications (2–6), thus making liver resection a challenging operation.

Planning systems for liver surgery use specific algorithms to identify relevant anatomic structures within images obtained through computed tomographic (CT) or magnetic resonance imaging. The most crucial step is the segmentation process,

consisting of the assignment of image voxels to anatomic structures. In fact, any kind of localized liver treatment requires the same information: fine liver surface segmentation, accurate detection of tumors, and precise vessel topography (7). Automatic liver segmentation is a challenging task, because the liver usually shares image intensity values with other nearby organs (eg, the kidneys), and the boundaries of target structures are generally not sharp (8). As a consequence, several liver segmentation methods have been implemented and validated in recent years, showing numerous possible compromises between segmentation accuracy, computational complexity, and the degree of algorithm automation (9–13).

In particular, a fully automatic method for the rapid segmentation of liver tissue and its internal lesions applied to CT scans was recently introduced by our research group (14). This method, validated on a series of patient data sets presenting different anatomic and pathologic situations, proved to be a robust and efficient tool for performing automatic segmentations of liver tissue and tumors that are very close to the manual contour drawing made by an expert radiologist and considered to be the gold standard.

The aim of this study was to present and evaluate a new algorithm for automatic segmentation of the hepatic vessel network, with the final goal of integrating our two algorithms in a single software tool for computer-assisted planning of liver surgery.

The accurate segmentation of liver vessels is fundamental for the successful outcome of several therapeutic liver treatments (15). In fact, the availability of robust preoperative planning systems based on precise and automatic identification of the hepatic vessel network would be very helpful for safely removing tumors located near major vessels (16,17). Furthermore, "in situ" ablation techniques (eg, cryoablation, radiofrequency ablation) are becoming increasingly important as alternatives to liver resection (18–21). These techniques also require precise vessel detection for suitable treatment planning and execution, because major hepatic vessels strongly influence the actual cancer cell destruction (22–26). Various approaches to liver vessel segmentation have been recently implemented and tested (1,27,28), but none of these methods has demonstrated the ability to maintain 100% sensitivity in the automatic identification of vessels < 3 mm in diameter and presenting the true morphologic configurations of a human liver.

To overcome these limitations, we developed a new vessel segmentation algorithm, specifically optimized to provide fully automatic and more sensitive identification of liver vessels on contrast-enhanced CT (CECT) images.

The effectiveness of our vessel segmentation approach was assessed on a CECT data set obtained from a liver phantom produced through stereolithography (STL), a rapid prototyping technique that allows the accurate fabrication of three-dimensional (3D) complex shapes starting from a 3D computer-aided design (CAD) model (29–33). In our case, the CAD model was derived from a real CECT acquisition of a human liver, so the resulting phantom (made of polymeric resin) had a "natural" and precisely known geometry, accurately reproducing the vessel network of a human liver along with the shape and volume of the surrounding parenchyma.

The automatic vessel segmentation performed by our algorithm on CECT images of the phantom was analytically compared to the measured features of the corresponding model to quantify the actual sensitivity and accuracy of our method for both single two-dimensional (2D) slices and 3D reconstruction of the hepatic vessel network.

MATERIALS AND METHODS

Liver Phantom Production Processes and Measurements

The liver phantom used in this study was fabricated through STL, an additive rapid prototyping technique that creates the desired object by exploiting the photopolymerization of a low-viscosity liquid resin and bonding the object sections, layer by layer. Using this fabrication methodology, complex shapes can be obtained on the basis of a direct link with a 3D CAD drawing of the object, leading to tailor-made or single functional parts that are efficiently and accurately realized (29–33).

The following sections are devoted to the description of liver CAD model preparation, features of the STL apparatus, and fabrication processes of the liver phantom, including specific measurements performed to take into account the accuracy of actual STL realization.

Liver CAD Model. A CECT liver data set acquired during a human subject scansion was used to produce the CAD model that was subsequently passed to the STL apparatus for phantom production.

The data set used was actually chosen from those collected for a previous research study (14) developed for a different purpose. The aforementioned study fully respected national privacy laws and had been also approved by the ethics committee. Adopted CT protocols followed the routine clinical protocols used in the involved hospitals for imaging the abdomen with portal vein phase of contrast enhancement.

In particular, the specific image data set used was acquired on a LightSpeed Pro 16 CT scanner (GE Medical Systems, Milwaukee, WI) located at the Interventional Center of the Rikshospitalet University Hospital (Oslo, Norway). Scanning acquisition parameters were as follows: voltage, 120 kV; x-ray tube current, 425 mA; exposure time, 707 ms; and slice thickness, 2.5 mm. A bolus of 150 mL of a nonionic contrast agent (Visipaque 320; Nycomed, Zurich, Switzerland) was administered intravenously.

Obtained CECT scan data were analyzed and processed through our previous algorithm (14), to automatically segment the liver volume, and through a semiautomatic tool for vessel segmentation, with the aim of obtaining a preliminary visualization of hepatic vessels. This segmentation procedure was then checked and manually refined by an expert operator, particularly ensuring the accurate segmentation of all liver vessels visible on the CECT images. The final result of the manual segmentation was stored as a sequence of Digital Imaging and Communications in Medicine images through MATLAB (The MathWorks, Natick, MA) and then converted into a single STL file using a public-domain image processing program (ITK-SNAP version 1.8; University of North Carolina at Chapel Hill, Chapel Hill, NC). This STL file represented the liver CAD model necessary for STL phantom production.

STL Apparatus. The STL apparatus (SLA 250; 3D Systems Inc, Rock Hill, SC) used for phantom production was composed of the following parts (see also Fig 1) and was used for our purposes according to the reported configuration:

- a He-Cd laser (Omnichrome series 3056; Omnichrome Laser and Electro-Optic Systems, Chino, CA) with a specific power of 17 mW/mm^2, emitting at a wavelength of 325 nm, with a beam diameter of 0.2 mm;
- a hardware and software scanning system that drives the laser beam on the surface of the liquid resin vat;
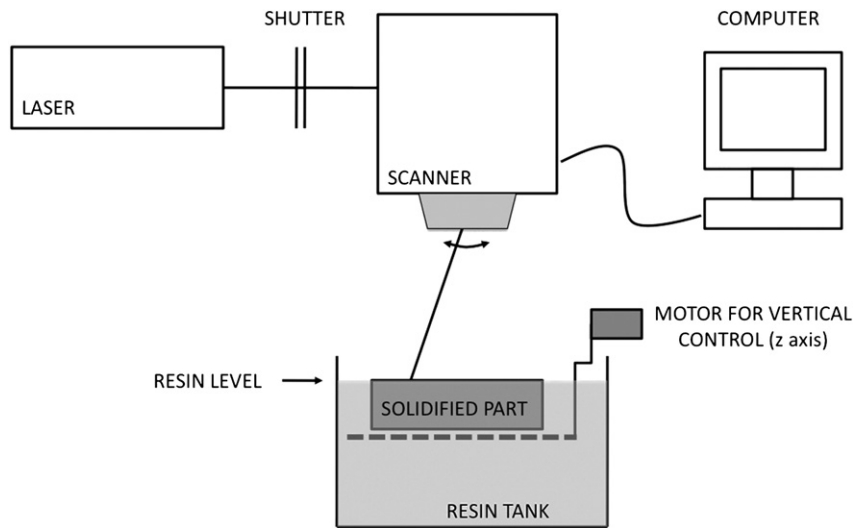
Figure 1. Scheme of the stereolithography apparatus.

- a computer-controlled platform that can be moved downward and upward along the object during the additive building procedure;
- an apparatus for resin recoating, operating before each layer building; and
- a tank filled with a commercial resin (RPC accuGen 100 HC; 3D Systems Inc) characterized by a suitable reactivity for use with a 325-nm laser source, to be polymerized when irradiated with an appropriate energy.

The CAD model file is acquired by the STL apparatus via file-transfer protocol from an external computer equipped with proprietary software (3D Lightyear; 3D Systems Inc), which converts the CAD model into a series of instructions for the object building process and allows all the corresponding parameter settings.

Liver Phantom Fabrication. Preliminary liver phantom fabrications on a reduced scale were used to define the best configuration of the STL production process and to test the related production accuracy. The final phantom realized with the full scale was built in four separate parts, to facilitate cleaning the vessel cavities of uncured resin. To do this, the aforementioned liver CAD model was divided into four separate portions by introducing three parallel and equally spaced "cutting planes" (see Fig 2). Each resulting model portion was saved as a new STL file and used as a CAD model for the building process of the corresponding liver phantom element.

After STL productions, all four elements were washed with isopropyl alcohol that was flushed by means of a syringe into each phantom cavity, to accurately remove unreacted resin. The same procedure was also used to remove excess resin from the external surfaces. Each phantom element was then postcured under a 325-nm ultraviolet lamp at room temperature (25°C), to obtain a fully hardened resin. The final phantom elements resulted stable over time under laboratory standard room conditions.
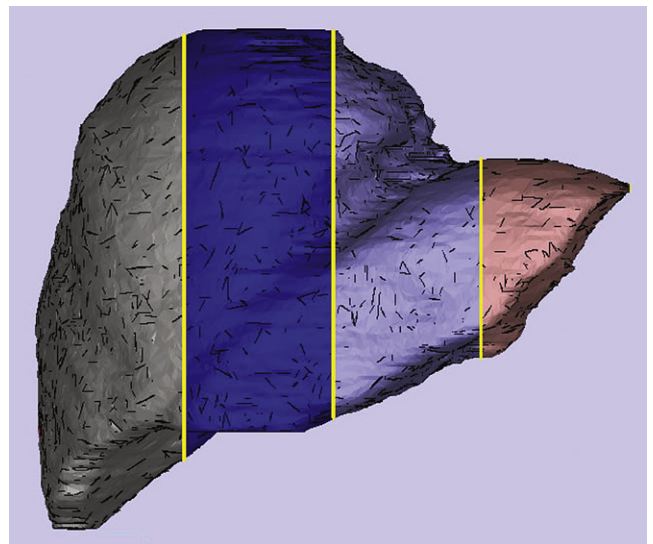

Figure 2. Liver computer-aided design model used for phantom production, showing the four constituent parts.

CAD Model Correction and Final Phantom Assembly. Before final phantom assembly, actual STL accuracy in realizing phantom vessels was specifically assessed on each manufactured phantom element, with the aim of obtaining a "corrected CAD model" perfectly identical to the produced phantom.

All the phantom element surfaces adjacent to a cutting plane were imaged through an image scanner (HP Officejet Pro L7680; Hewlett-Packard Corporation, Palo Alto, CA), and vessel section areas were manually segmented in the six resulting images using ImageJ software (National Institutes of Health, Bethesda, MD). Values of segmented areas were then compared with those obtained by performing the same manual segmentation on the corresponding CAD model

images, and, for each vessel section, a surface correction factor k was calculated using the following formula:

$$k = \frac{A_{\text{phantom}}}{A_{\text{model}}}, \tag{1}$$

where A_{phantom} is the vessel section area measured on phantom images, and A_{model} is the area of the same vessel section measured on the CAD model. The k values obtained for each vessel section were averaged over each of the six images considered, and the average of the resulting six mean values was assumed as the correction factor for vessel section areas throughout the entire phantom.

The four phantom parts produced were finally assembled by bonding each one to the others using a silicon sealant, and after 24 hours, the phantom was ready to be used. A picture of the phantom is reported in Figure 3.

Acquisition of CECT Images

Phantom Filling Procedure. To facilitate the introduction of contrast solution into the phantom vessels, both phantom access channels (corresponding to the hepatic vein and the portal vein) were equipped with a syringe slightly inserted into the hole and fixed in a vertical position by means of a silicon sealant.

The phantom was then filled with a saline–diluted solution of a nonionic contrast agent (Ultravist 300; Schering AG, Berlin, Germany) prepared by adding 12 mL of Ultravist 300 (containing 300 mg iodine/mL) to 100 mL of sodium chloride (0.9%), because this concentration would suitably simulate the contrast agent level present in the liver during the venous phase of a typical clinical CECT examination (personal communication from an expert radiologist). The solution obtained was also labeled with a small amount of methylene blue to allow an easy visual check of contrast solution presence in each phantom vessel.

Finally, to eliminate air bubbles from the vessels and to ensure optimal filling, the contrast-filled phantom was placed inside a chamber of a lyophilizator equipped with a vacuum pump (LIO 5P 4k, 5 Pa; Trezzano sul Naviglio, Milan, Italy) for 30 minutes. A picture of the contrast-filled phantom is shown in Figure 4.

Image Acquisition. Helical CT scans were performed using a 64-slice CT scanner (Aquilion 64; Toshiba Medical, Tokyo, Japan), using the following parameters (corresponding to a standard protocol for abdominal acquisition): voltage, 120 kV; x-ray tube current, 428 mA; gantry rotation time, 0.55 seconds; collimation, 0.5 mm; reconstruction interval, 0.5 mm; exposure time, 700 ms; reconstruction filter, FC 13; pixel size, 0.625×0.625 mm; image matrix, 512×512; and slice thickness, 0.5 mm.

During CT scanning, the phantom was placed in an open plastic box with its seam production planes aligned with the x-ray transmission direction, to minimize possible image artifacts due to such discontinuities. The acquired data were saved in Digital Imaging and Communications in Medicine format.

Image Segmentation and Experimental Optimization of Algorithm Configuration

A new fully automatic custom-developed software program was used for phantom image segmentation from Digital Imaging and Communications in Medicine data. This software was obtained from combining our previous tool for segmentation of liver tissue (14) with a new algorithm for automatic vessel segmentation. In particular, our vessel segmentation algorithm is based on a custom ITK implementation and optimization of the vesselness filter method (34), as briefly summarized herein.

A Hessian matrix and corresponding eigenvalues $|\lambda_1(\sigma)| \leq |\lambda_2(\sigma)| \leq |\lambda_3(\sigma)|$ are computed for each image voxel at a scale σ, corresponding to a certain sought vessel size, providing information on the contrast between the regions inside and outside the range $(-\sigma, \sigma)$ along each principal direction. Then, for each voxel, the following vesselness function is calculated:

$$v = \begin{cases} 0 & \text{if } \lambda_2 > 0 \text{ or } \lambda_3 > 0 \\ \left[1 - \exp\left(-\frac{R_A^2}{2\alpha^2}\right)\right] \cdot \exp\left(\frac{R_B^2}{2\beta^2}\right) \\ \quad \cdot \left[1 - \exp\left(-\frac{S^2}{2c^2}\right)\right] & \text{otherwise} \end{cases}, \tag{2}$$

where

$$R_A = \frac{|\lambda_2|}{|\lambda_3|}, \tag{3}$$

$$R_B = \frac{|\lambda_1|}{\sqrt{|\lambda_2 \cdot \lambda_3|}}, \tag{4}$$

$$S = \sqrt{\lambda_1^2 + \lambda_2^2 + \lambda_3^2}, \tag{5}$$

and α, β, and c are constant coefficients having the following values: $\alpha = 0.5$, $\beta = 0.5$, and $c = 5$.

The vesselness function is expected to provide the higher values only for voxels belonging to bright tubular structures (ie, vessels), characterized by $\lambda_2 \approx \lambda_3 < 0$ and $\lambda_1 \approx 0$ (with $|\lambda_1| << |\lambda_2|$).

In our case, the vesselness function was evaluated for eight different values of σ, approximately covering the range of all phantom vessel diameters (0.2–16 mm). We assumed as final vesselness of each image voxel the value obtained as

$$v_0 = \max_\sigma v(\sigma). \tag{6}$$

Finally, the value of v_0 for each image voxel was compared with an experimentally determined threshold parameter T to decide whether the considered voxel had to be depicted as a vessel voxel in the final output image. At the end of the segmentation process, the segmented liver structures could
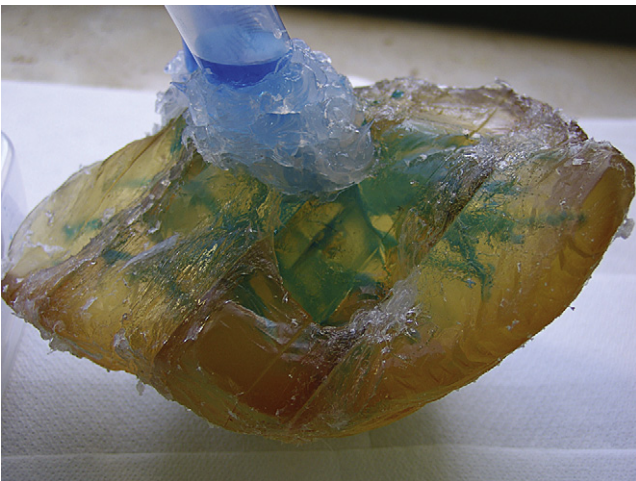
Figure 3. The realized phantom.

Figure 4. The liver phantom after the contrast filling procedure.

be viewed either as a 3D object or as a sequence of 2D slices through ITK-SNAP.

Actually, σ was expressed in voxel units (with the minimum possible value being 1.0 voxel), and for each vessel voxel, maximum vesselness value was expected at the scale that approximately matched the vessel diameter. Therefore, we expected some problems in detecting vessels whose diameters were below the voxel dimension, as detailed in the "Discussion" section.

The optimal T value was determined by comparing the total volume of phantom vessels, measured on the corrected CAD model through the software Myriad 3D Reader (Informative Graphics Corporation, Scottsdale, AZ) and in principle equivalent to the volume of venous blood in the liver, with the total volume of the vessels obtained from automatic segmentation of phantom CT images by using different T values. The T value that generated a segmented vessel volume coincident with the value measured on the corrected CAD model was selected as the optimal T value. The resulting

accuracy of the vessel segmentation carried out through our algorithm using the selected T value was then evaluated in detail, as described in the next paragraph.

Techniques for Segmentation Accuracy Evaluation

The accuracy of the developed vessel segmentation method was evaluated by considering both the 3D features of the vessel tree and the single 2D liver slices and by comparing them to the "ground truth," which for the former (3D vessel tree) was represented by the corrected 3D CAD model and for the latter (2D slices) corresponded to the CT images manually segmented by an experienced operator. Details of the specific methodologies adopted to assess the quality of vessel segmentation are provided in the following sections.

Three-Dimensional Analysis of the Segmented Vessel Tree. Both the automatically segmented and the model-derived liver vessel trees were divided into two main segments, corresponding to the main branches of the hepatic vein and the portal vein, respectively, and the vessel subsegments of each main branch were labeled hierarchically. In this way, vessel subsegments up to the fourth order were identified in both vessel trees.

The sensitivity of the segmentation algorithm used was evaluated as a function of vessel diameter and vessel order, by identifying in each case the percentage of correctly segmented vessels in all those physically present in the phantom, taking as reference the corrected CAD model.

Therefore, for each vessel order and diameter range considered, sensitivity percentage was calculated according to the following formula:

$$\text{sensitivity} = \frac{\text{TP}}{\text{TP} + \text{FN}}, \tag{7}$$

where TP represents the true-positives (ie, phantom vessels that were correctly segmented by the algorithm) and FN the "false-negatives" (ie, phantom vessels that were not identified by the algorithm).

Two-Dimensional Analysis of Liver Slices. To perform an accurate and more local evaluation of algorithm effectiveness in reproducing the precise morphology of segmented vessels, we also compared the results of manual and automatic segmentation on four parallel equally spaced liver phantom slices, each one representing the "median slice" of the corresponding phantom element.

Two values were obtained for the area of each vessel section present in the liver slices: one was measured on the automatically segmented CECT image, and the other was obtained from manual segmentation of the same CECT slice performed by an experienced operator.

As recommended by Altman and Bland (35), agreement between the two methods was assessed by calculating the paired difference for each measurement and by estimating the bias (mean difference) and 95% limits of agreement (2 standard deviations around the mean difference) relative to the average measurement of both methods. In addition to the Bland-

Altman statistics, Pearson's correlation coefficient (r) was calculated as a measure of consistency between the two methods.

Moreover, suitable metrics for comparing 2D shapes of vessel sections derived from automatic and manual segmentations were adapted to the specific purpose of this study from our previous work (14) and were used to further quantify vessel segmentation accuracy. For each vessel section, the overlapping area was assessed by calculating the Dice similarity coefficient (DSC), the false-positive ratio (FPR), and the false-negative ratio (FNR), respectively, defined as follows:

$$DSC = \frac{2(M_1 \cap A_1)}{M_1 + A_1}, \tag{8}$$

$$FPR = \frac{2(M_0 \cap A_1)}{M_1 + A_1}, \tag{9}$$

and

$$FNR = \frac{2(M_1 \cap A_0)}{M_1 + A_1}, \tag{10}$$

where A and M represent, respectively, automatic and manual segmentation, and 1 and 0 correspond, respectively, to the consideration of vessel and parenchyma pixels.

RESULTS

CAD Model Correction

To obtain a CAD model perfectly identical to the vessel tree of the phantom, vessel sections in each slice of the original CAD model were "corrected" through multiplication by the experimentally determined correction factor $k = 0.941$.

The resulting "corrected CAD model" was used as a "gold standard" for the subsequent evaluations of vessel segmentation accuracy on the basis of the analysis of the 3D vessel tree.

Optimization of Algorithm Threshold Parameter

The optimal value of the segmentation threshold parameter T was determined as the value that minimized the difference between the total volume of the segmented liver vessel tree and the corresponding volume measured on the corrected CAD model.

Figure 5 shows the curve obtained by plotting the aforementioned volume difference as a function of the T value used; it can be observed that the difference goes to zero for $T = 2059$.

The effects of different T values on vessel segmentation is also qualitatively shown in Figure 6, illustrating the results of manual and automatic segmentation on a typical liver CT slice, with emphasis on the differences between the automatic segmentation performed with the optimal threshold ($T = 2059$) and the same operation conducted with a lower or higher T value.
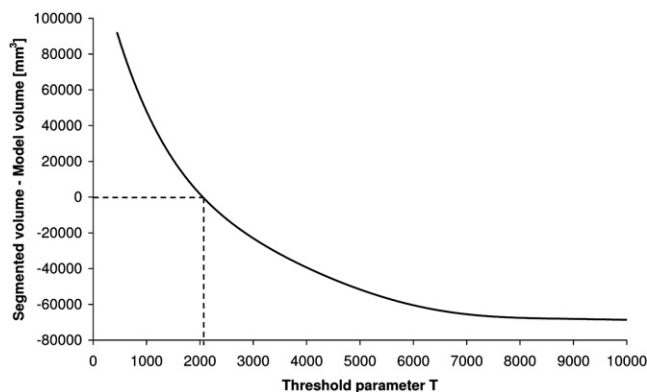

Figure 5. Plot of the difference between the total volume of the segmented liver vessel tree and the corresponding volume measured on the corrected computer-aided design model as a function of the T value used (dashed lines identify the optimal parameter setting).

In particular, from Figure 6a, it can be noted how using too low a threshold (eg, $T = 500$) overestimates all the vessel sections and causes the appearance of "additional vessels" (false-positives) not actually present in the scanned phantom. On the contrary, using too high a threshold (eg, $T = 5000$) underestimates all the vessel sections and does not allow detection of the smallest vessels (false-negatives).

These effects are further highlighted in Figures 6b and 6c, respectively reporting the zoom shots of the areas labeled 1 and 2 in Figure 6a. Figure 6b shows how too low a T value can misinterpret a group of small vessels as a single larger one, and Figure 6c points out the case in which a single large vessel is erroneously split into a set of smaller vessels because of too high a T value.

Automatic segmentation performed at $T = 2059$ globally showed a very good concordance with the manual segmentation results; therefore, this value was selected as the optimal threshold for automatic segmentation of liver vessels from CECT images.

Figure 7 shows the 3D image resulting from the automatic segmentation performed on our phantom using the selected value of threshold parameter ($T = 2059$). The accuracy of this segmentation was then specifically quantified through the previously described evaluation techniques, whose results are reported in the following paragraphs.

Three-Dimensional Analysis of the Segmented Vessel Tree

Sensitivity analysis of the implemented segmentation methodology was carried out by comparing the segmented vessel tree with the corrected CAD model, separately analyzing vessel diameters and vessel subsegment order.

Regarding vessel diameter, as reported in Figure 8, sensitivity was 14% for very small subsegment branches with diameters in the range 0.2 to 0.5 mm and increased to 50% for branches 0.5 to 1 mm in diameter. Sensitivity was 100% for all branches in the range 1 to 16 mm.
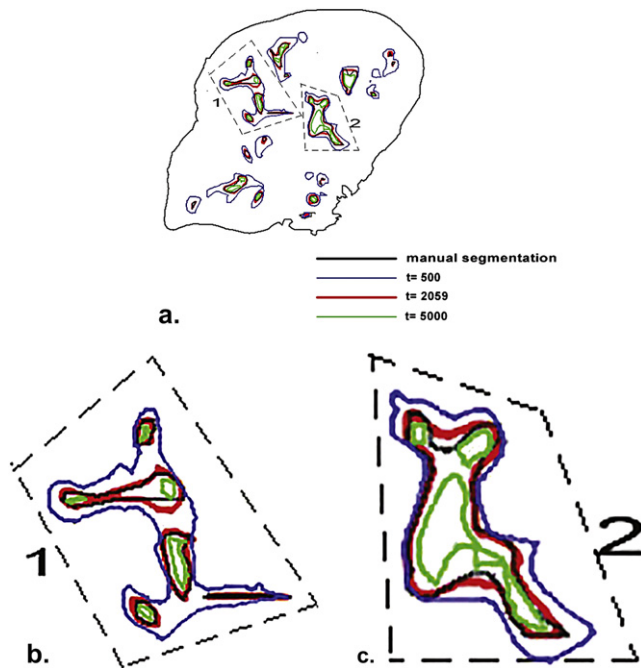
Figure 6. Effect of the adopted *T* value on the accuracy of the vessel segmentation obtained: **(a)** global effect on a typical liver slice; **(b)** zoom shot of area 1, showing how the use of too low a *T* value causes the misinterpretation of a group of small vessels as a single larger one (blue line); **(c)** zoom shot of area 2, showing how too high a *T* value causes the erroneous splitting of a single large vessel into a set of smaller ones (green lines).
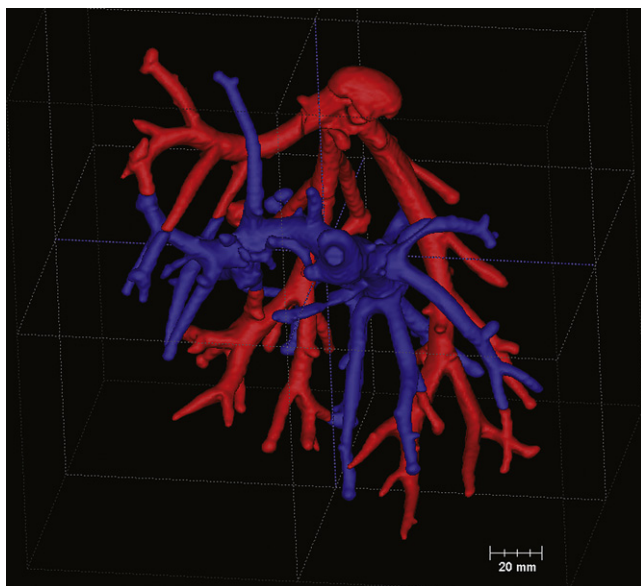

Figure 7. Result of the automatic phantom image segmentation (*T* = 2059).

In relation to subsegment order, as reported in Figure 9, sensitivity was 100% for first-order branches, and it decreased to 88%, 80%, and 70%, respectively, for second-order, third-order, and fourth-order branches.

The number of branches in the phantom for each subsegment order was also counted and is reported in Table 1, along
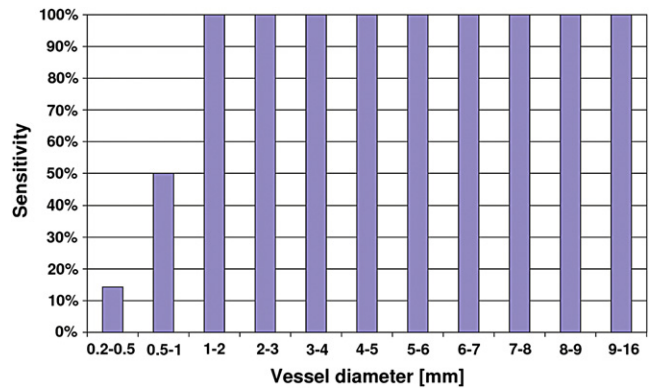

Figure 8. Sensitivity of the vessel segmentation algorithm against vessel diameter (percentage of segmented vessels with respect to the actual phantom vessels).
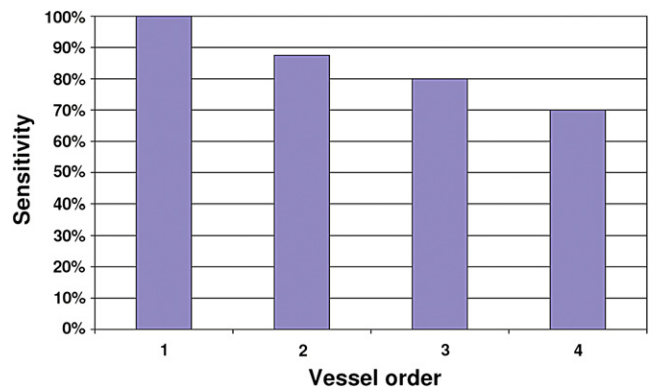

Figure 9. Sensitivity of the vessel segmentation algorithm against vessel order (percentage of segmented vessels with respect to the actual phantom vessels).

with the corresponding diameter ranges and the number of vessels that were correctly identified by the algorithm.

Two-Dimensional Analysis of Liver Slices

The level of agreement between manual and automatic liver vessel segmentation was quantified by measuring the corresponding vessel section areas on various 2D liver slices and using Bland-Altman statistics, Pearson's correlation coefficient, and the calculus of three metrics (DSC, FPR, and FNR).

Figure 10 shows the Bland–Altman plot obtained, in which the average error in vessel section area (expressed as bias $\pm$ 2 standard deviations) was 0.06 ± 8.41 mm^2. Pearson's correlation coefficient, assumed as a measure of consistency, was found to be 0.997. For a graphical representation, the scatterplot of vessel section areas is reported in Figure 11, together with the line of unity.

This good level of accuracy was also confirmed by the values of the calculated metrics. In fact, automatically segmented vessel sections overlapped the great majority of the corresponding real phantom ones with significant robustness (DSC = 94.9 $\pm$ 6.5%). Furthermore, the algorithm achieved an FPR of 7.7

TABLE 1. Number of Vessels in the Phantom and Number of Vessels Identified by the Automatic Segmentation Algorithm, Grouped by Corresponding Subsegment Order

	Vessel Order				
	1 (9.8–16.0 mm)	2 (0.4–9.4 mm)	3 (0.5–3.1 mm)	4 (0.2–2.0 mm)	Total
Phantom vessels	2	16	15	10	43
Segmented vessels	2	14	12	7	35
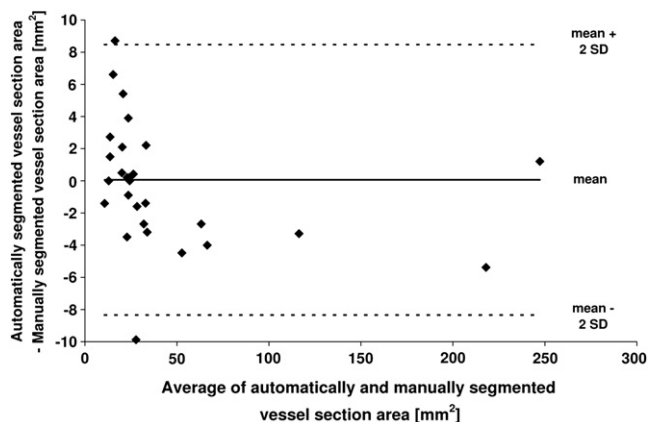
Figure 10. Bland-Altman plot for comparison of automatically and manually segmented vessel section areas.

Figure 11. Scatterplot showing the performed measurements of vessel section areas. The line of equality is also shown.

$\pm$ 13.7% and an almost ideal FNR (2.3 $\pm$ 4.1%), indicating the substantial absence of undetected vessel voxels.

DISCUSSION

Routine clinical planning of surgical liver resection usually involves the schematic classification of various liver segments. However, in many cases the liver's complex internal anatomy differs markedly from commonly adopted classifications (eg, Couinaud classification) (3–5). In all of these cases, the surgeon is obliged to imagine the 3D liver structure on the basis of a multitude of 2D images (typically several hundred for high-resolution CT scans), and this complex task is one of the main reasons for the difficulty of liver resection.

The recent introduction of computer planning systems offers a new way to identify relevant anatomic structures within liver diagnostic images. The final output of such systems is the display of a virtual 3D liver model on a computer screen, allowing a surgeon to perform navigation in virtual volumes, all possible rotations, zoom shots, and volume calculations (36,37), with a consequent increase in surgical precision (38–43).

The most crucial step in computer-based planning of liver surgeries is the segmentation process, in particular the segmentation of liver vessels, which is of fundamental importance for accurate intervention planning but at the same time can be subject to several significant errors.

In this study, we assessed an innovative software tool for automatic segmentation of the hepatic vessel network from a CECT liver scan, evaluating the actual effectiveness of our algorithm through an experimental study on a highly precise
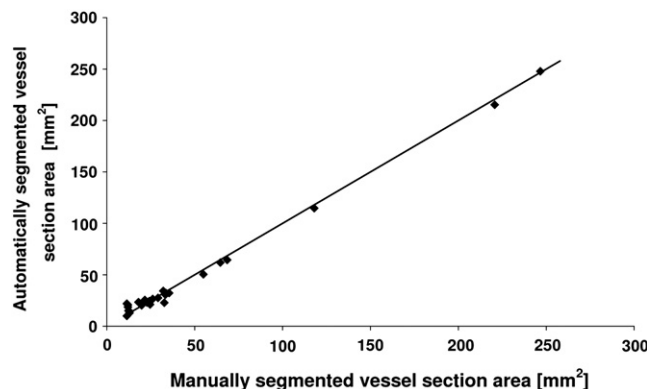
phantom reproduction of a human liver, for which all morphologic details and boundary conditions were known in detail "a priori."

After experimental definition of the most suitable threshold parameter, to optimize the accuracy of the implemented algorithm, we quantified the algorithm performance in two independent ways: (1) 3D analysis of global sensitivity on the basis of vessel tree assessment and (2) detailed 2D pixel-based statistical analyses on vessel sections present in single CT slices.

In our first analysis, we compared the 3D vessel tree resulting from automatic segmentation of our contrast-filled phantom to the corresponding vessel tree obtained from the corrected CAD model used for phantom production. We counted 43 vessel branches in the corrected CAD model, which were subdivided into 11 groups according to diameter (range, 0.2–16 mm) and classified in four different vessel subsegment orders. Sensitivity in relation to the vessel diameter (Fig 8) was particularly high, with 100% of vessels with diameters > 1 mm correctly identified. Then, as expected, sensitivity decreased to 50% for vessels in the range 0.5 to 1 mm (comparable to the imaging system resolution), and residual 14% sensitivity was maintained for vessels < 0.5 mm (ie, less than the physical pixel-related resolution). Nevertheless, some omitted small vessels were not optimally filled by contrast solution, so actual algorithm sensitivity in the detection of vessels < 1 mm in presence of "ideal" contrast filling is expected to be somewhat higher anyway with respect to the aforementioned values.

Sensitivity in relation to vessel subsegment order (Fig 9) started with 100% for first-order vessels and then progressively

decreased for higher order vessels. However, this is only due to an increasing proportion of small vessels with increasing vessel order, while we verified that all vessels > 1 mm were correctly segmented at least up to the fourth order, independently of the angle in which they originated from the corresponding parent vessels and of any other specific morphologic condition. Moreover, narrow vessels with diameters < 1 mm are unlikely to have significant clinical importance during liver resection planning.

The achievement of 100% sensitivity in the fully automatic detection of all vessels with diameters > 1 mm, independent of vessel subsegment order and specific morphologic conditions, is a remarkable result, considering that recently reported alternative methods for analogous purposes used phantoms with simplified vessel geometries (27), reached detection sensitivities close to 100% only for vessels with diameters > 3 mm (1), or required operator interaction to correctly identify vessels with diameters < 4 mm (28).

Our additional 2D analysis was conducted on single equally spaced CT slices sampled all along the phantom and aimed to determine the actual accuracy of the implemented segmentation method in reproducing the precise shape of each identified vessel. Again, our approach achieved very good results, because the average DSC index, accounting for the degree of overlap between automatically and manually segmented areas, was $94.9 \pm 6.5\%$, and Pearson's correlation coefficient, measuring the consistency between the two segmentation methods, was 0.997. In addition, the very low value of FNR ($2.3 \pm 4.1\%$) indicated the substantial absence of undetected vessel voxels, while the higher value of FPR ($7.7 \pm 13.7\%$), coupled with the positive value of the average error in vessel section area (0.06 mm^2, corresponding to a percentage error of 4.73%), documented that in most cases, automatically segmented vessels resulted slightly larger than corresponding real ones. This is an intrinsic feature of our methodology, which in case can be tuned by optimizing the threshold parameter T using an "augmented" vessel volume instead of the actual one. This represents a further advantage in view of possible clinical use, because our software can automatically provide a minimum safety margin around the real vessels, and this can be particularly useful when planning specific liver interventions.

CONCLUSIONS

We developed a new fully automatic method for the 3D segmentation of all liver structures (parenchyma, vessels, and, if present, tumors) from CECT scans, resulting from the combination of a previously validated tool for segmentation of liver volume and hepatic tumors (14) with a new algorithm for automatic vessel segmentation, whose effectiveness has been experimentally evaluated in the present work.

The vessel detection sensitivity of our algorithm was excellent, even compared to recently reported results of different tools for analogous purposes, showing the unprecedented ability to correctly segment all liver vessel branches > 1 mm in diameter, at least up to the fourth subsegment order and

regardless of specific morphologic conditions. Accuracy in the precise reproduction of identified vessel morphology was also very high, with the possibility of including a tunable safety margin around each segmented vessel.

We therefore conclude that our liver segmentation software, including tools for parenchyma identification and internal lesion detection, is a promising computer system for supporting 3D planning of liver surgery and guiding intraoperative resections.

Future developments will include exploring strategies to improve algorithm sensitivity in detecting vessels < 1 mm and experimental studies to optimize the threshold parameter for planning liver surgeries that require specific safety margins.

REFERENCES

1. Lehmann KS, Ritz J-P, Valdeig S, et al. Portal vein segmentation of a 3D-planning system for liver surgery—in vivo evaluation in a porcine model. Ann Surg Oncol 2008; 15:1899–1907.
2. Coinaud C. Le foie: etudes anatomiques et chirurgicales. Paris, France: Masson, 1957.
3. Fasel JHD, Selle D, Evertsz CJG, et al. Segmental anatomy of the liver: poor correlation with CT. Radiology 1998; 206:151–156.
4. van Leeuwen MS, Fernandez MA, van Es HW, et al. Variations in venous and segmental anatomy of the liver: two- and three-dimensional MR imaging in healthy volunteers. AJR Am J Roentgenol 1994; 162:1337–1345.
5. Fischer L, Cardenas C, Thorn M, et al. Limits of Coinaud's liver segment classification: a quantitative computer-based three-dimensional analysis. J Comput Assist Tomogr 2002; 26:962–967.
6. Fischer L, Thorn M, Neumann JO, et al. The segments of the hepatic veins—is there a spatial correlation to the Coinaud liver segments? Eur J Radiol 2005; 53:245–255.
7. Lamata P, Lamata F, Sojar V, et al. Use of the Resection Map system as guidance during hepatectomy. Surg Endosc 2010; 24:2327–2337.
8. Massoptier L, Casciaro S. Segmentation of liver anatomy and pathology. In: Casciaro S, Samset E, eds. Novel technologies for minimally invasive therapies. Lecce, Italy: Lupiensis Biomedical Publications, 2007; 57–66.
9. Masutani Y, Uozumi K, Akahane M, et al. Liver CT image processing: a short introduction of the technical elements. Eur J Radiol 2006; 58: 246–251.
10. Saitoh T, Tamura Y, Kaneko T. Automatic segmentation of liver region based on extracted blood vessels. Syst Comput Japan 2004; 35:633–641.
11. Lamecker H, Lange T, Seebaß M. Segmentation of the liver using a 3D statistical shape model. ZIB Technical Report 04-09. Berlin, Germany: Zuse Institute Berlin, 2004.
12. Okada T, Shimada R, Hori M, et al. Automated segmentation of the liver from 3D CT images using probabilistic atlas and multilevel statistical shape model. Acad Radiol 2008; 15:1390–1403.
13. Liu F, Zhao B, Kijewski PK. Liver segmentation for CT images using GVF snake. Med Phys 2005; 32:3699–3706.
14. Massoptier L, Casciaro S. A new fully automatic and robust algorithm for fast segmentation of liver tissue and tumors from CT scans. Eur Radiol 2008; 18:1658–1665.
15. Sboarina A, Foroni RI, Minicozzi A, et al. Software for hepatic vessel classification: feasibility study for virtual surgery. Int J Comput Assist Radiol Surg 2010; 5:39–48.

16. Kamiyama T, Nakagawa T, Nakanishi K, et al. Preoperative evaluation of hepatic vasculature by three-dimensional computed tomography in patients undergoing hepatectomy. World J Surg 2006; 30:400–409.

17. Hansen C, Zidowitz S, Hindennach M, et al. Interactive determination of robust safety margins for oncologic liver surgery. Int J Comput Assist Radiol Surg 2009; 4:469–474.

18. Osada S, Yoshida K, Saji S. A novel strategy by cryoablation for advanced hepatoma. Anticancer Res 2009; 29:5203–5209.

19. Elhawary H, Oguro S, Tuncali K, et al. Multimodality non-rigid image registration for planning, targeting and monitoring during CT-guided percutaneous liver tumor cryoablation. Acad Radiol 2010; 17:1334–1344.

20. Fagnoni FF, Zerbini A, Pelosi G, et al. Combination of radiofrequency ablation and immunotherapy. Front Biosci 2008; 13:369–381.

21. Meijerink MR, van Waesberghe JH, van der Weide L, et al. Early detection of local RFA site recurrence using total liver volume perfusion CT: initial experience. Acad Radiol 2009; 16:1215–1222.

22. Frericks BB, Ritz JP, Albrecht T, et al. Influence of intrahepatic vessels on volume and shape of percutaneous thermal ablation zones: in vivo evaluation in a porcine model. Invest Radiol 2008; 43:211–218.

23. Albrecht D, Germer CT, Isbert C, et al. Interstitial laser coagulation: evaluation of the effect of normal liver blood perfusion and the application mode on lesion size. Lasers Surg Med 1998; 23:40–47.

24. Frericks BB, Ritz JP, Roggan A, et al. Multipolar radiofrequency ablation of hepatic tumors: initial experience. Radiology 2005; 237:1056–1062.

25. Isbert C, Roggan A, Ritz JP, et al. Laser-induced thermo-therapy: intra- and extralesionary recurrence after incomplete destruction of experimental liver metastasis. Surg Endosc 2001; 15:1320–1326.

26. Ritz JP, Isbert C, Roggan A, et al. Laser-induced thermo-therapy of liver metastases. Front Radiat Ther Oncol 2004; 38:106–121.

27. Esneault S, Lafon C, Dillenseger J-L. Liver vessels segmentation using a hybrid geometrical moments/graph cuts method. IEEE Trans Biomed Eng 2010; 57:276–283.

28. Kaftan JN, Tek H, Aach T. A two stage approach for fully automatic segmentation of venous vascular structures in liver CT images. In: Pluim JPW, Dawant BM, eds. Medical imaging 2009: image processing. Orlando, FL: SPIE, 2009. 725911-1–12.

29. Greco A, Esposito Corcione C, Maffezzoli A. Temperature evolution during stereolithography building with a commercial epoxy resin. Polym Eng Sci 2006; 46:493–502.

30. Greco A, Licciulli A, Maffezzoli A. Stereolithography of ceramic suspensions. J Mater Sci 2001; 36:99–105.

31. Corcione C, Greco A, Montagna F, et al. Silica moulds built by stereolithography. J Mater Sci 2005; 40:4899–4904.

32. Licciulli A, Corcione C, Greco A, et al. Laser stereolithography of ZrO_2 toughened Al_2O_3. J Eur Ceramic Soc 2005; 25:1581–1589.

33. Corcione C, Montagna F, Greco A, et al. Free form fabrication of silica moulds for aluminum casting by stereolithography. J Rapid Prototyping 2006; 12:184–188.

34. Frangi AF, Niessen WJ, Vincken KL, et al. Multiscale vessel enhancement filtering. In: Wells WM, Colchester A, Delp SL, eds. Berlin, Germany: Springer Verlag, 1998; 130–137.

35. Altman DG, Bland JM. Measurements in medicine: the analysis of method comparison studies. Statistician 1983; 32:307–317.

36. Frericks BB, Caldarone FC, Nashan B, et al. 3D CT modeling of hepatic vessel architecture and volume calculation in living donated liver transplantation. Eur Radiol 2004; 14:326–333.

37. Radtke A, Nadalin S, Sotiropoulos GC, et al. Computer-assisted operative planning in adult living donor liver transplantation: a new way to resolve the dilemma of the middle hepatic vein. World J Surg 2007; 31:175–185.

38. Lang H, Radtke A, Hindennach M, et al. Impact of virtual tumor resection and computer-assisted risk analysis on operation planning and intraoperative strategy in major hepatic resection. Arch Surg 2005; 140:629–638.

39. Lamade W, Glombitza G, Fischer L, et al. The impact of 3-dimensional reconstructions on operation planning in liver surgery. Arch Surg 2000; 135:1256–1261.

40. Frericks BB, Kirchhoff TD, Shin HO, et al. Preoperative volume calculation of the hepatic venous draining areas with multi-detector row CT in adult living donor liver transplantation: impact on surgical procedure. Eur Radiol 2006; 16:2803–2810.

41. Lang H, Radtke A, Liu C, et al. Extended left hepatectomy-modified operation planning based on three-dimensional visualization of liver anatomy. Langenbecks Arch Surg 2004; 389:306–310.

42. Fuchs J, Warmann SW, Sieverding L, et al. Impact of virtual imaging procedures on treatment strategies in children with hepatic vascular malformations. J Pediatr Gastroenterol Nutr 2010; 50:67–73.

43. Takahashi K, Sasaki R, Kondo T, et al. Preoperative 3D volumetric analysis for liver congestion applied in a patient with hilar cholangiocarcinoma. Langenbecks Arch Surg 2010; 395:761–765.